Acta Materialia 227 (2022) 117696

Contents lists available at ScienceDirect

Acta Materialia

journal homepage: www.elsevier.com/locate/actamat

Giant compliance and spontaneous buckling of beams containing mobile solute atoms

Jörg Weissmüller[a,b,*], Shan Shi[a,b]

[a] Institute of Materials Physics and Technology, Hamburg University of Technology, Hamburg, Germany
[b] Institute of Materials Mechanics, Helmholtz-Zentrum Hereon, Geesthacht, Germany

ARTICLE INFO

Article history:
Received 14 November 2021
Revised 26 January 2022
Accepted 27 January 2022
Available online 29 January 2022

Keywords:
Mechanics
Open-system elasticity
Chemo-mechanical coupling
Larché–Cahn theory
Gorsky-effect
Nonlinear elasticity

ABSTRACT

Recent experiments have shown that the elastic compliance of a porous metal can be substantially enhanced when mobile solute is alloyed into interstitial sites of the crystal lattice. The observations agree with predictions – due to Gorsky and to Larché and Cahn – for the elasticity of open systems in which the elastic responses is probed at constant chemical potential. The underlying mechanism involves an exchange of solute between tensile and compressive fibers in beam-like elements of the microstructure. Here, we analyze the elastic deformation of such elements in a continuum approach, accounting explicitly for the coupling between chemistry and mechanics. We consider a regular solution with linear elasticity in the limit of constant composition and with a linear composition-strain coupling. Materials parameters are matched to experiments on Pd-H, so as to realistically account for the balance between chemical and mechanical energies. At constant chemical potential, the elastic response can be strongly nonlinear. With decreasing temperature, the bending goes from a monotonic moment-curvature relation to one including a horizontal tangent and, hence, a state of giant bending compliance. Reducing the temperature further brings first a temperature interval with a simple bistability and finally one with degeneracy including – depending on the chemical potential or on the mean solute fraction – the possibility of finite curvature at zero moment. Quenching the uniform solution into a two-phase region of the alloy phase diagram can lead to spontaneous buckling at no load. Furthermore, degenerate moment-curvature relations allow for bending states in which the radius is not a constant along the beam axis. Intervals of lar ge strain at constant load are similar to superelasticity, but the underlying phase transformation is here not martensitic.

1. Introduction

When a solid body containing mobile solute atoms is exposed to external load, then changes in the chemical potential that result from the stress prompt the internal redistribution of the solute and/or the exchange of solute with an external reservoir. This was first considered by Gorsky [1] in his analysis of the elastic after-effect in a beam-bending scenario, where the overall composition is constant but larger atoms diffuse from the compressed toward the expanded fibre of the beam. Gorsky's considerations underly "Gorsky-effect" experiments investigating the kinetics of hydrogen diffusion in metals [2,3]. The more general case of a continuum with arbitrary geometry and load distribution has been treated in a seminal paper by Larché and Cahn [4]. These authors investigated a nonuniformly stressed solid that can exchange solute at equilibrium with a reservoir at constant chemical potential. They showed that the chemical potential in the solid remains uniform at the value of the reservoir. Focusing on the linear elastic response at small strain, they further showed that the stress- and strain fields obey the classic laws of mechanics, yet with the conventional elastic parameters – applicable at constant composition – replaced by open-system elastic parameters. On top of the spontaneous elastic response of Hooke's law, those parameters account for the extra strain that comes with the change in composition in reaction to the stress. Consistent with the Le Chatelier–Brown Principle [5], the extra configurational degree of freedom that is the displacement of solute will invariably act to enhance the elastic compliance. While the underlying concepts are well acknowledged and are explicitly or implicitly considered in many modeling

* Corresponding author at: Institute of Materials Physics and Technology, Hamburg University of Technology, Hamburg, Germany.
E-mail address: weissmueller@tuhh.de (J. Weissmüller).

https://doi.org/10.1016/j.actamat.2022.117696

approaches [6–13], it is only quite recently that experiments have started exploring the open-system elastic parameters [14].

Experimental investigations of the Gorsky effect observe the elastic response on two separate timescales: jumps in the external load on a macroscopic body entail the immediate elastic response at constant composition, followed by the much slower (time constants ~ 1 h for mm-size bodies [15,16]) strain of the "elastic after-effect". Diffusion constants of the mobile solute species may be inferred from the time-dependence of the slower process. Yet, when the redistribution of solute is confined to the scale of nanometers, the time constant for that process comes down to < 1 ms [14]. That situation prevails in nanoporous metals, which take the form of networks of nanometer-scale struts that deform locally in bending when the macroscopic sample is exposed to an external uniaxial compression or tension [17–20]. Indeed such materials, when alloyed with hydrogen as a mobile solute, exhibit enhanced elastic compliance in quantitative agreement with the predictions of the Larché–Cahn theory [14]. The elastic response of the open system then appears spontaneous in experimental studies at frequencies up to 100 Hz. Rather than exploring diffusivity, such experiments strive for tuning of the elastic response of the material through the incorporation of mobile solute.

As a remarkable property of the elastic response of open systems, theory predicts a strongly nonlinear stress-strain response [21]. This prediction reflects the inherent nonlinearity of equations of state for the chemical potential of solutions as the function of their composition, as it originates from the composition-dependence of the entropy of solution. Solute-solute interaction terms also contribute. As it is related to the entropy, the open-system elastic response also varies strongly with the temperature. So far, dedicated experiments on the elastic response of open systems have been limited to small strain and discussed in terms of the leading, linear term in the stress-strain response [14]. Yet, the higher-order behavior should be relevant to experiments and open to investigation.

Of particular interest are solid solutions with a miscibility gap that closes at a critical point. Near that point, changes in the composition leave the energy invariant to first order, while the strain remains a linear function of the composition. There may then be deformation that costs no energy, resulting in particularly interesting phenomena for the simultaneous mechanical and chemical equilibrium [14].

The prerequisite for the phenomenon of open-system elastic softening is that a material can take up mobile solute molecules that give rise to strain (or swelling). This process is found in such diverse materials as polymers [22], gels [23], or plant tissue [24] that equilibrate with water vapor at different relative humidity, and in lithium ion battery cathodes that incorporate Li by intercalation [25]. Yet, the most extensive empirical data in the context involves metal hydrides [26,27]. Their hydrogen content is readily controlled by equilibration with H_2 gas at controlled partial pressure or with a protic electrolyte at controlled electrode potential. Hydrides of palladium, its alloys, or niobium have well-documented equations of state for their alloy chemistry, and values of the H partial molar volume - which governs the chemo-mechanical coupling strength - are precisely known for those systems [28–31]. Furthermore, their solid solutions with H typically do exhibit miscibility gaps with experimentally accessible critical points [29,31,32].

With an eye on experiments exploring beam-bending scenarios at the nanoscale, this study analyzes the open-system elasticity of beams, allowing specifically for nonlinear elastic behavior. Focussing on the simplest relevant model scenario, we consider an isotropic and linear elastic crystal containing mobile solute atoms. The chemistry is that of a regular solution. Chemistry and mechanics are coupled, and the question to be answered is: when the chemical potential is held constant, what are the stress-strain relations at equilibrium and what are the associated elastic parameters? Specifically, we shall work this out first for uniaxial tension/compression of a prismatic bar, looking at the open-system Young's modulus, and second for the bending of a beam of constant cross-section, looking at the open-system bending stiffness. Attention is restricted to equilibrium states, and time-dependent phenomena are ignored. Materials parameters matched to Pd–H are used in numerical evaluation; in this way the observations are expected to reflect realistic effects, by magnitude. The analysis concludes with a brief and, again, qualitative discussion of how the results for beam bending can be transferred to experiments – such as Ref [14] – that use nanoporous metals for implementing and studying open-system elasticity.

2. Constitutive assumptions

We consider an elastic solid solution and assume that a local Helmholtz free energy density, Ψ (free energy per volume), depends on temperature, T, solute density, ρ, and strain as the state variables. For simplicity, we limit attention to uniaxial stress states, which we describe by the stress magnitude, σ. The strain magnitude (strain projected on the stress axis) is designated by ε. Furthermore, we introduce the solute fraction, x, as the composition variable, and take $\rho = x\rho_0$ with ρ_0 a density of sites available for solute.

The assumptions so far let us identify T, ε, and x as the state variables for Ψ. Since all variations and processes of interest to this study are at constant temperature, we can effectively treat T as a label; for conciseness its display is suppressed whenever appropriate. The fundamental equation is then

$$\mathrm{d}\Psi = \sigma\,\mathrm{d}\varepsilon + \mu\rho_0\mathrm{d}x\,, \tag{1}$$

with μ the solute chemical potential. Here, we have assumed that ρ_0 is a constant. The underlying concept is that of the network solid of Larché and Cahn [4], in which the network (for instance, the host atom crystal lattice) provides an invariable reference frame in which interstitial solute can diffuse. Consistent with this assumption, we use Lagrangian variables throughout, measuring all densities in coordinates of the undeformed state. Then, σ is a 2nd Piola-Kirchhoff stress [33].

We note that there is, in principle, nothing wrong with applying the approach of this work also to substitutional solutions, now replacing μ with the diffusion potential (the difference between the chemical potentials of the two substitutional components [34]). Yet, the kinematics then require that both constituents, solute as well as solvent, can diffuse. In a practical experimental scenario it is then nonobvious how the network constraint – namely an invariable reference frame for diffusion and strain – can be maintained. It is for that reason that the discussion is here restricted to interstitial solutions.

3. Young's modulus - open versus closed system

For elastic deformation at constant composition, the relevant elastic parameter is the conventional, constant-composition Young's modulus,

$$Y = \mathrm{d}\sigma/\mathrm{d}\varepsilon|_x\,. \tag{2}$$

Yet, when the solute can be redistributed and exchanged at equilibrium with an external reservoir of solute at chemical potential μ, then the elastic parameter is the open-system Young's modulus,

$$\hat{Y} = \mathrm{d}\sigma/\mathrm{d}\varepsilon|_\mu\,. \tag{3}$$

Here we briefly derive the relation between Y and $\hat{Y}$ based on our constitutive assumptions; that relation is one of the central results of the Larché–Cahn theory [4].

In view of Eq. (3), the quantity to be evaluated can be taken as the increment in strain, $\mathrm{d}\varepsilon$, in response to an increment in stress, $\mathrm{d}\sigma$, at constant chemical potential μ. We can start out by decomposing the strain into a response to stress at constant composition plus a response to composition change at constant stress:

$$\mathrm{d}\varepsilon = \frac{\mathrm{d}\varepsilon}{\mathrm{d}\sigma}|_x \mathrm{d}\sigma + \frac{\mathrm{d}\varepsilon}{\mathrm{d}x}|_\sigma \mathrm{d}x\,. \tag{4}$$

Next, we evaluate $\mathrm{d}x$, which is the change in solute fraction while the stress is varied at constant chemical potential,

$$\mathrm{d}x = \frac{\mathrm{d}x}{\mathrm{d}\sigma}|_\mu \mathrm{d}\sigma\,. \tag{5}$$

We then realize that Eq. (1) implies the Maxwell relation

$$\frac{\mathrm{d}x}{\mathrm{d}\sigma}|_\mu = \frac{1}{\rho_0}\frac{\mathrm{d}\varepsilon}{\mathrm{d}\mu}|_\sigma\,, \tag{6}$$

and we apply the chain rule to a term on the right-hand side of that equation, in the form

$$\frac{\mathrm{d}\varepsilon}{\mathrm{d}\mu}|_\sigma = \frac{\mathrm{d}\varepsilon}{\mathrm{d}x}|_\sigma \frac{\mathrm{d}x}{\mathrm{d}\mu}|_\sigma\,. \tag{7}$$

Combining the above results, we obtain a result for the quantity of interest, in the form

$$\frac{\mathrm{d}\varepsilon}{\mathrm{d}\sigma}|_\mu = \frac{\mathrm{d}\varepsilon}{\mathrm{d}\sigma}|_x + \left(\frac{\mathrm{d}\varepsilon}{\mathrm{d}x}|_\sigma\right)^2 \frac{1}{\rho_0}\frac{\mathrm{d}x}{\mathrm{d}\mu}|_\sigma\,. \tag{8}$$

We can now combine Eq. (8) with the definitions of Y and $\hat{Y}$. Furthemore, we can define the concentration-strain coefficient as $\eta = \mathrm{d}\varepsilon/\mathrm{d}x|_\sigma$ and a solute susceptibility parameter as $\chi = \rho_0^{-1}\mathrm{d}x/\mathrm{d}\mu|_\sigma$ [4]. In terms of those quantities, we finally obtain

$$\frac{1}{\hat{Y}} = \frac{1}{Y} + \chi\eta^2\,, \tag{9}$$

or, equivalently,

$$\hat{Y} = \frac{Y}{1+\chi\eta^2 Y}\,. \tag{10}$$

This is one of the results of Ref. [4], here derived along a different (simpler) route.

In experiment, Y and η may often be approximated as constants within the interesting domain in the parameter space (T, ε, x), and we shall use that approximation consistently throughout this work. Yet, as will be apparent below, one must generally allow for χ to undergo large variation as the function of T, σ, and μ. It then follows that $\hat{Y}$ will also vary strongly with T, with ε or σ, and with x or μ. The key issue in this work is to discuss these variations and their ramifications for stress/strain or bending-moment/curvature relations, which will generally be nonlinear. We shall base the discussion on the simplest equations of state that yield the central materials phenomena.

4. Equations of state

4.1. Mechano-chemical coupling

We consider all relevant interstitial sites as identical. We take the solute to cause an isotropic dilatation of the crystal lattice, so that the macroscopic strain tensor $\mathbf{E}$ in the stress-free state relates to the solute fraction x by

$$\mathbf{E} = \eta\mathbf{U}x\,, \tag{11}$$

with $\mathbf{U}$ the unit tensor in 3D. Recall that we take η as constant, independent of x or σ.

As a consequence of the above assumption, changes in composition cannot result in shear. Conversely, the chemical potential is independent of shear components of the stress state and only dependent on the stress through the trace of the stress tensor – in other words, through the pressure [4].

In an elastically isotropic and infinitely extended solid body, an isotropic center of dilatation (here: a misfitting solute atom) induces a strain field that is pure shear outside of the inclusion [35]. Hence, the long-range strain field makes no contribution to η in the infinitely extended isotropic solid. Yet, the misfit strain tensor field of a solute atom in a solid of finite extension – irrespective of its size – may contain non-vanishing diagonal entries, which contribute to η and to the solute-solute interaction. Obviously, each and every experimental situation will involve such bodies of finite extension. The solute-induced lattice strain at $\eta \neq 0$ will forcefully induce a solute-solute interaction energy with a convex composition dependence [8,36–39]. This favors unmixing. In other words, the presence of a miscibility gap in the alloy phase diagram is systematically correlated with the atomic size misfit and, thereby, with the interaction between chemistry and mechanics.

On top of the elastic solute-solute interaction, there are also electronic contributions. These may favor either, mixing or unmixing. Yet, the elastic contribution is often strong, and it dominates the phase behavior in many important alloy systems [38].

4.2. Stress-strain relation and reference state

As stated above, we assume – for constant composition – linear and isotropic elasticity and we focus specifically on uniaxial stress. Representing the stress-strain behavior in terms of $\varepsilon(\sigma, x)$ we then have the equation of state

$$\varepsilon = \frac{\sigma}{Y} + \eta x\,, \tag{12}$$

with Y Young's modulus at constant composition.

Here, as consistently throughout the following, we have explicitly assumed Y to be independent of the composition. Furthermore, we have taken the stress-free crystal at zero solute content as the reference state for strain. That reference state will also be used consistently throughout this work.

4.3. Chemical potential

The simplest scenario that is consistent with the universal behavior of solutions in their limits of high dilution and of the approach to saturation while also featuring a miscibility gap that closes in a critical point is that of a regular solution [40] with, at uniform pressure P, an attractive solute-solute interaction. In other words, the solute-solute interaction energy parameter, ω_P, at constant P needs to be positive-valued. The equation of state for the chemical potential, μ, is here (Porter et al. [40] and see Wagner [41] for the pressure-dependence)

$$\mu = \omega_\mathrm{P}(1-2x) + RT\ln\frac{x}{1-x} + 3\eta\Omega P\,. \tag{13}$$

Here, R denotes the molar gas constant and $\Omega = 1/\rho_0$ the matrix volume per interstitial site.

For the example of interstitial solute on the octahedral sites of a face-centered cubic crystal, such as H in Pd, the number of matrix atoms and interstitial sites agree. Ω is then the atomic volume of the matrix crystal. Note that this scenario is also consistent with isotropic dilatation, as assumed above.

The regular solution has a miscibility gap that closes at the critical temperature, T_C, which satisfies

$$T_\mathrm{C} = \frac{\omega_\mathrm{P}}{2R}\,. \tag{14}$$

Fig. 1 displays the miscibility gap in the alloy phase diagram (see below for reduced units). Below T_C, the solvus line (solid line in the

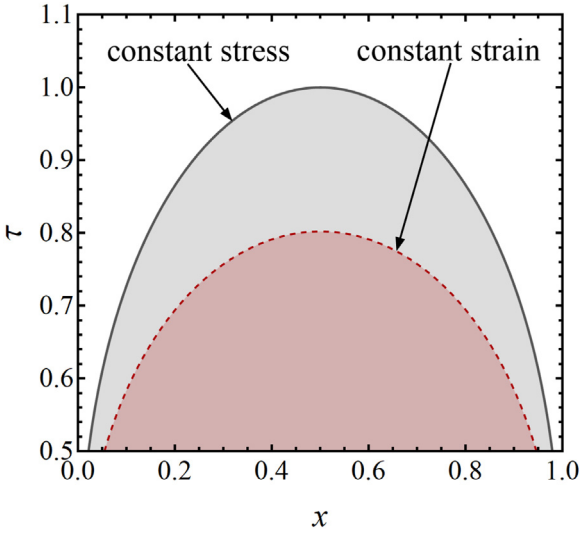

Fig. 1. Alloy phase diagrams of the regular solution in the domain of solute fraction, x, versus reduced temperature (temperature relative to the critical temperature of the miscibility gap at constant-stress), τ. Boundary conditions: constant stress (gray, solid line) and constant strain (red, dashed line). Below the respective critical temperature – i.e., at reduced temperatures $\tau < 1$ for constant stress and at $\tau < 1 - \eta^2 y/2 \approx 0.80$ for constant strain – a dilute phase is separated from a concentrated one by a miscibility gap (shaded regions). Materials parameters η and y motivated by Pd–H, see main text. (For interpretation of the references to color in this figure legend, the reader is referred to the web version of this article.)

figure) separates the domain in {composition, temperature} space where the uniform solid solution is stable from a domain in which, at thermodynamic equilibrium, a dilute (in solute) phase coexists with a concentrated one.

Applying the above statements to the scenario with uniaxial stress, we obtain an equation of state for the chemical potential as the function of T, x, σ in the form[1]

$$\tilde{\mu}_\sigma(T, x, \sigma) = \omega_P(1-2x) + RT \ln \frac{x}{1-x} - \eta\Omega\sigma \,. \tag{15}$$

Eqs. (13) and 15 imply that the solute susceptibility parameter χ for use with Eqs. (9) and 10 obeys

$$\chi = \frac{x(1-x)\Omega}{RT - 2x(1-x)\omega_P} \,. \tag{16}$$

Note that χ is here completely determined by x, with no explicit dependency on the acting stress or strain.

In the stress-free limit, the open-system Young's modulus $\hat{Y}$ at equilibrium is expected to vanish at the critical point, $T = T_C$ and $x = 1/2$ [14]. For $T < T_C$, $\hat{Y}$ is also expected to vanish at the spinodals [14].

We are also interested in situations with controlled strain not stress (Helmholtz-type versus Gibbs-type). Solving Eq. (12) for σ and inserting into Eq. (15) yields an equation of state for μ as the function of T, x, ε:

$$\tilde{\mu}_\varepsilon(T, x, \varepsilon) = \omega_P(1-2x) + RT \ln \frac{x}{1-x} - \eta\Omega Y(\varepsilon - \eta x) \,. \tag{17}$$

This can be brought into the analogous form as Eq. (15) by defining an effective interaction energy, ω_ε, for constant strain,

$$\omega_\varepsilon = \omega_P - \frac{1}{2}\eta^2\Omega Y \,, \tag{18}$$

in terms of which

$$\tilde{\mu}_\varepsilon(T, x, \varepsilon) = \omega_\varepsilon(1-2x) + RT \ln \frac{x}{1-x} - \eta\Omega Y(\varepsilon - \frac{\eta}{2}) \,. \tag{19}$$

[1] We denote equations of state by a tilde, so as to distinguish functions from parameter values.

Since $\eta^2\Omega Y$ is positive definite, Eq. (18) implies that going from constant stress to constant strain makes ω less positive. In the consequence, the upper convolute temperature, T_ε, of the alloy phase diagram at uniform strain is reduced as compared to the critical temperature of the conventional, uniform stress scenario. The solvus line of the modified phase diagram is displayed by the dashed line in Fig. 1.

Why emphasize the distinction between uniform-stress and uniform-strain scenarios? We are interested in discussing both, the tensile (or compressive) deformation of a bar and the bending deformation of a beam. For the bar in tension or compression, the equilibrium equations of mechanics require that the stress is uniform. In other words, stress is our control variable here and we want to know the resulting strain. By contrast, the simplest geometry for the beam is bending into a segment of circle of constant curvature. That geometry fixes the strain field, and we need to evaluate the stress that results from that strain. Here, strain is our control variable and we want to know the stress. The two scenarios above address these two distinct tasks and each plays a vital role in the analysis below.

5. Materials parameters and reduced variables

We aim to inspect the phenomenology of open-system elastic deformation qualitatively, yet with an eye on a rough assessment of realistic magnitudes of effects. To this end, we select the values of the two relevant materials parameters (to be introduced below) to roughly match the Pd–H system [29,42]. In that system, hydrogen atoms occupy octahedral interstitial sites in the face-centered cubic lattice of the host, palladium. Consistent with the alloy phase diagram of Fig. 1, Pd–H exhibits a continuous series of solid solutions at high temperature and, below a critical temperature, a miscibility gap that separates a dilute phase from a concentrated one. Hydrogen uptake expands the crystal lattice, with an essentially linear relation between composition and lattice parameter. The alloy chemistry and the mechanics of Pd–H are not in all details caught by the idealized equations of state introduced in the previous Section. For instance, Pd is elastically anisotropic [43], and its solution thermodynamics is affected by the limited number of empty d-band states, restricting the hydrogen content to $x \lesssim 0.6$ under practical conditions [29,32,44]. Yet, the numbers provide an appropriate basis for realistically assessing the approximate magnitude of effects.

The values adopted here are: lattice parameter of the face-centered cubic lattice 389.0 pm [45], critical temperature of the miscibility gap $T_C = 566$ K [44,46], (polycrystalline) Young's modulus $Y = 120$ GPa [43], concentration-strain coefficient $\eta = 0.060$ [30,47]. Then, based on T_C and Eq. (14), $\omega_P \approx 10$ kJ/mole ≈ 0.10 eV.

As a preliminary for introducing reduced variables, we find it useful to define a chemical energy density variable, θ as

$$\theta = \omega_P/\Omega \,. \tag{20}$$

The relative magnitude of characteristic chemical and mechanical energy densities is then parameterized by the reduced Young's modulus parameter,

$$y = Y/\theta \,, \tag{21}$$

and the coupling strength between chemistry and mechanics is parameterized by η. These dimensionless parameters form the basis for a more general reduced notation, which is summarized in Table 1.

In terms of that notation, the equations of state take the form (see footnote [1])

$$\tilde{\varepsilon}(x, s) = \frac{s}{y} + \eta x \,, \tag{22}$$

Table 1
Reduced quantities: definitions and values or ranges. Symbols for original quantities used in the definitions: state variables μ - chemical potential, P - pressure, σ - stress, T - temperature, ε - strain; materials parameters ω_P - solute-solute interaction energy parameter, Ω - solvent atomic volume, Y - Youngs modulus; beam-related parameters d - beam thickness, I - cross-sectional area moment of inertia, κ - curvature, M - bending moment. R is the molar gas constant.

	Quantity	Symbol/defining equation	Value/range
state variable	solute fraction	x	$0 \dots 1$
	chemical potential	$m = \mu/\omega_P$	$-\infty \dots +\infty$
	temperature	$\tau = T/T_C$	> 0
	(uniaxial) stress	$s = \sigma/\theta$	$<> 0$
	pressure	$p = P/\theta$	$<> 0$
	strain	ε	$<> 0$
materials parameter	critical temperature	$T_C = 2R/\omega_P$	irrelevant (> 0)
	chemical energy density	$\theta = \omega_P/\Omega$	irrelevant (> 0)
	concentration-strain coefficient	η	0.060
	Young's modulus	$y = Y/\theta$	110
beam-related parameters	radial position	$\zeta = z/d$	$-1/2 \dots 1/2$
	neutral fibre position	ζ_0	$<>0$
	curvature	$k = \kappa d$	> 0
	bending moment	$\mathfrak{m} = Md/(I\theta)$	$<> 0$
	mean solute fraction	$\bar{x}$	> 0

$$\tilde{s}(x, \varepsilon) = (\varepsilon - \eta x)\, y\,, \tag{23}$$

$$\tilde{m}_s(\tau, x, s) = (1 - 2x) + \frac{\tau}{2} \ln \frac{x}{1-x} - \eta s\,, \tag{24}$$

and

$$\tilde{m}_\varepsilon(\tau, x, \varepsilon) = \left(1 - \frac{y\eta^2}{2}\right)(1 - 2x) + \frac{\tau}{2} \ln \frac{x}{1-x} - \eta y\left(\varepsilon - \frac{\eta}{2}\right). \tag{25}$$

It is seen that only two materials parameters are of relevance, namely η, which measures the strength of coupling between strain and composition, and y, which compares the characteristic magnitudes of the mechanical and the chemical energy densities. Furthermore, the temperature parameter τ weights the importance of the entropy, which favors mixing, and the interaction energy, which favors unmixing.

As stated above, Fig. 1 shows alloy phase diagrams for the regular solution, as it is described by Eqs. (24) and (25). The phase diagrams illustrate specifically that the upper convolute temperature of the two-phase coexistence regime in the constant-strain case, τ_ε, is substantially below that of the uniform-stress case, $\tau_C = 1$. With the materials parameters of our study, $\tau_\varepsilon = 1 - y\eta^2/2 \approx 0.80$.

The presence of two-phase regions in the equilibrium alloy phase diagram reflects the observation that the isotherms of composition versus chemical potential can be multivalued. At constant stress, there can be multiple solutions (in x) of $m = \tilde{m}_s(\tau, x, s)$ at temperatures below T_C, as exemplified in Fig. 2(a). When going from constant stress to constant strain, one finds the isotherms (now $\tilde{m}_\varepsilon(\tau, x, \varepsilon)$) modified. Here, multiple solutions are observed only at temperatures below the lower critical value, T_ε, as exemplified in Fig. 2(b). In each case, only regions of positive slope in $x(m)$ correspond to stable or metastable states of the alloy. In regions of negative slope (dashed lines in the figure), the open system is spinodally unstable. When there are multiple solutions, the alloy can be in a two-phase state. The coexisting phases have different composition but identical stress (Fig. 2(a)) or identical strain (Fig. 2(b)). As the function of the phase fraction, one can then find the mean composition anywhere between the compositions of the coexisting phases. That range of compositions is marked by the shaded regions in the figure.

The considerations, in our analysis, of local chemical and mechanical equilibrium are sufficient to establish states of the system as metastable. Deciding upon the nature of the stable state under the acting set of boundary conditions requires an inspection of the minimum in the appropriate total free energy function. This is not part of the scope of our analysis. In experiments, phase transformations typically involve hysteresis, for instance due to nucleation barriers or to the limited mobility of internal interfaces. These phenomena then govern the selection of the state within the two-phase region. Again, the relevant phenomenology is outside the scope of our present discussion.

The different phase behavior under uniform strain as compared to uniform stress has many well-established analogies in materials science. They comprise the distinction between the chemical and the coherent spinodal [48], situations of coherent phase equilibrium [8,49–51] and speficially the depression of the critical temperature in thin metal hydride films clamped to a rigid substrate [52–54] and the suppression of the critical temperature of hydride nanoparticles [55,56].

6. Phase transformations and lattice coherency

At two-phase coexistence, the distinct phases of a crystalline solid – such as Pd–H – are often separated by an incoherent interface. Generating the interface entails finite jumps in the displacement field and discrete changes in the materials points' nearest neighbor relations. That is not compatible with the network constraint of Ref. [4] or with the use of reference coordinates in our analysis.

Here, we restrict attention to scenarios where any phase transformation is coherent. Such scenarios are encountered, for instance, during precipitation in single-crystalline superalloys [8,57], in coherent spinodal decomposition [48] and, significantly, in nanoscale metal hydrides [51,53,54]. For our benchmark system Pd–H, coherent phase transformations have been documented in nanoparticles [56] and in nm-thin films [53,58], and the observation of > 1000 cycles through the phase transformation without apparent microstructural changes also points towards coherent two-phase coexistence in the nanoporous material [47].

7. Tensile stress-strain relation

Here, we wish to display the graph of strain versus stress at constant chemical potential. In terms of Eq. (22), this requires eval-

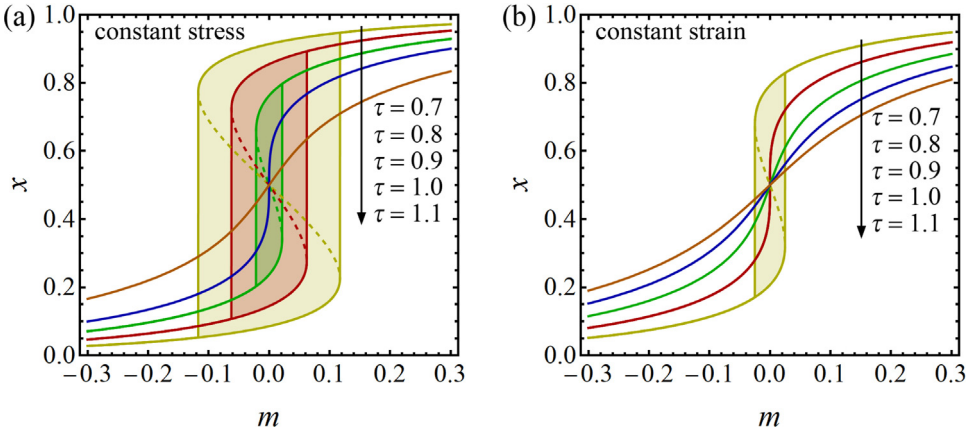

Fig. 2. Exemplary plots of solute fraction x in the regular solution versus reduced chemical potential m at (a) constant stress, here $s = 0$, and (b) constant strain, here $\varepsilon = \eta/2$. Reduced temperatures $\tau = 0.7$ (yellow), $\tau = 0.8$ (red), 0.9 (green), 1.0 (blue) and 1.1 (orange). Shaded regions mark metastable states of two-phase coexistence at intermediate values of m for $\tau < 1$ in (a) and for $\tau < 0.8$ in (b). Dashed: unstable branches of $m(x)$ at the lower τ. (For interpretation of the references to color in this figure legend, the reader is referred to the web version of this article.)

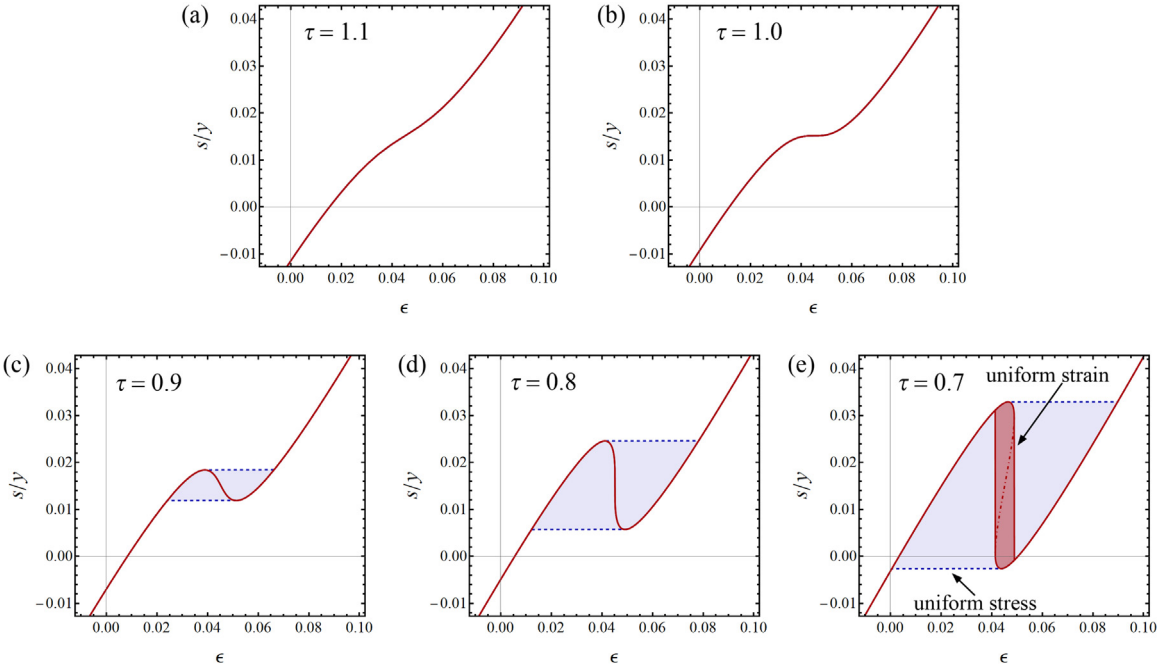

Fig. 3. Stress normalized to Young's modulus, s/y, versus strain, ε, at constant chemical potential, μ, and at uniform stress (blue, dashed, largely covered by red line) or at uniform strain (red, solid). Exemplary plot, here for $\mu = -0.1$ and for reduced temperatures $\tau = 1.1$ (a), 1.0 (b), 0.9 (c), 0.8 (d) and 0.7 (e). Shaded regions mark two-phase states at uniform stress (blue) or uniform strain (red). Under constant-stress conditions, two-phase states exist for all temperatures below T_C (below $\tau = 1$, here for figure parts (c)–(e)). By contrast, uniform-strain conditions allow for two-phase coexistence only at temperatures that are below T_ε by a finite interval (here below $\tau = 0.8$, figure part (e) only). Dash-dotted red: unstable solution of Eq. (27) at uniform strain. (For interpretation of the references to color in this figure legend, the reader is referred to the web version of this article.)

uating the functions

$$\tilde{\varepsilon}(\tau, m, s) = \frac{s}{y} + \eta\, \tilde{x}_s(\tau, m, s)\,. \tag{26}$$

for uniform stress conditions or

$$\tilde{s}(\tau, m, \varepsilon) = y\,(\varepsilon - \eta\, \tilde{x}_\varepsilon(\tau, m, \varepsilon)) \tag{27}$$

for uniform strain. As the inverse functions of Eqs. (24) and (25) for $\tilde{m}_s(\tau, x, s)$ or $\tilde{m}(\tau, x, \varepsilon)$, respectively, the functions $\tilde{x}_s(\tau, m, s)$ and $\tilde{x}_\varepsilon(\tau, m, \varepsilon)$ in the above equations are not available in closed form and so require numerical evaluation. We used an algebra program (Mathematica v12.1) for this as for all other numerical evaluations of this work. The numerical analysis was set up to track multiple solutions for x whenever present.

Fig. 3 compares constant-chemical-potential stress-strain relations at uniform stress to those at uniform strain. The example is for $m = -0.1$ which, at low τ, puts the stress-free system in the dilute phase and close to the two-phase coexistence region in the alloy phase diagram. Recall that, depending on the boundary conditions, two-phase coexistence states can take different forms, two regions of identical stress but different strain or to two regions of identical strain but different stress. The figure shows that the stress-strain curves for these scenarios can be quite different, the constant strain condition is more restrictive and results in a substantially narrower two-phase region. This reflects the difference in the phase diagrams, see Fig. 1 above, and in the isotherms of the chemical potential, see Fig. 2(a) versus 2(b).

Fig. 3 illustrates that three regimes may be distinguished:

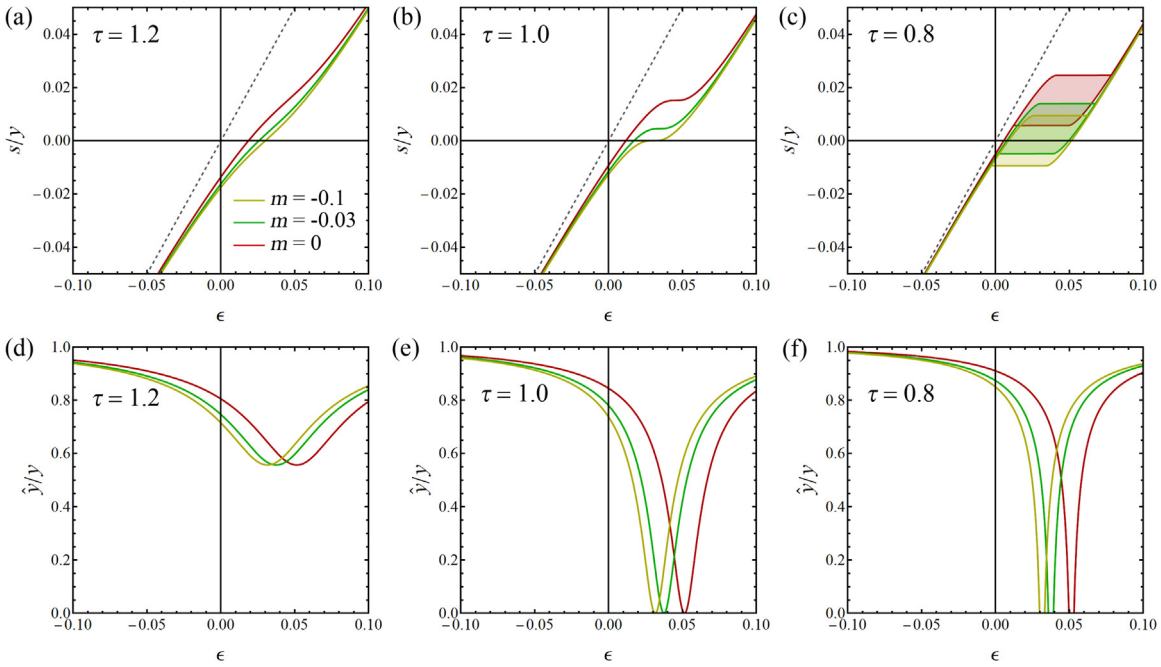

Fig. 4. Axial deformation of a prismatic bar at uniform axial stress and constant chemical potential. Stress (normalized to Young's modulus), s/y, versus strain, ε (a–c) and open-system Young's modulus (normalized to the constant-composition one), $\hat{y}/y$, versus strain (d–f). Reduced temperatures $\tau = 1.2$ (a,d), 1.0 (b,e) and 0.8 (c,f). Reduced chemical potentials $m = -0.1$ (yellow), -0.03 (green) and 0 (red). Dashed gray line: stress-strain relation at constant composition. (For interpretation of the references to color in this figure legend, the reader is referred to the web version of this article.)

- In the regime $\tau > 1$ (here $\tau = 1.1$ in Fig. 3a) the stress-strain graph increases monotonously.
- At $\tau = 1$ (Fig. 3b) the stress-strain graph for the first time exhibits a horizontal tangent. This corresponds to a point around which the leading term in the stress-strain relation is a third-order polynomial. In other words, Young's modulus vanishes and the compliance diverges.
- In the regime $\tau < 1$ (exemplified here by $\tau = 0.9$ in Fig. 3c) the stress-strain graphs are degenerate. The graph at uniform stress reflects two-phase coexistence (blue shaded region). By contrast, the graph at uniform strain here reflects single-phase behavior at any strain, yet with a point of inflection.
- At $\tau = \tau_\varepsilon$ (here $\tau \approx 0.8$, Fig. 3d) the stress-strain graph for the first time exhibits a vertical tangent.
- In the regime $\tau < \tau_\varepsilon$ (here $\tau = 0.7$ in Fig. 3e) the stress-strain graph for any boundary condition, uniform stress as well as uniform strain, exhibit the multiple branches that represent two-phase states. Regions with identical stress but different strain or with identical strain but different stress (blue and red shaded areas in the graph, respectively) can then coexist.

Next, we inspect exemplary stress-strain and Young's-modulus-strain relations at different combinations of τ and m. Here we have in mind a prismatic bar with axial loads applied to its ends, in other words, a situation of uniform stress. Figs. 4(a)–(c) exemplify stress-strain relations obtained by evaluating Eq. (26). Note that all stress-strain graphs exhibit a finite strain at zero stress; this is a consequence of our choice of the reference state (see Section 4.2). The graphs confirm that the open system (solid lines) is more compliant than the closed one (dashed lines). Furthermore, the graphs provide further illustrations of the behavior discussed above.

Fig. 4 (d)–(f) display the prediction of Eq. (10) for the open-system Young's moduli (here shown normalized to the constant-composition one) at the stress states of Fig. 4(a)–(c). Minima, points of vanishing stiffness, and regions of elastic instability ($Y < 0$, outside the range of the figure) may be discerned. These features reflect the variation of the solute susceptibility parameter χ in Eq. (10) with the solute fraction x, as it is implied by Eq. (16) along with the function $\tilde{x}_\varepsilon(\tau, \varepsilon, m)$ and the imposed values of τ, ε and m.

8. Beam bending

8.1. Geometry and stress field

Here we consider bending of a long beam of constant and (specifically, for simplicity) rectangular cross-section of height d and width w within the Euler–Bernoulli approach. The beam is bent along a radius aligned with the height coordinate, z. We take the beam to be slender, i.e. the ratio w/d is sufficiently small so that tensile stress components can be approximated as uniaxial, exclusively in the axial direction [59]. Consistent with the notation so far, we designate that stress component by σ. We maintain the use of Lagrangian coordinates, in other words, all position coordinates are measured in the reference configuration defined by the stress-free state with no solute.

The bending geometry is such that the strain in the axial direction–we designate that strain component by ε–satisfies

$$\varepsilon = (z - z_0)\kappa \,, \tag{28}$$

with κ the bending curvature (the inverse of the bending radius) and z_0 the position of the neutral (no strain) fibre. Note that composition change at no bending results in uniform strain; a neutral fibre can then not be defined. Note also that finite solute fraction and small curvature will typically result in a neutral fibre position outside the beam.

We define the coordinates so that $z = 0$ at the centroid of the beam cross-section; the beam extends by $\pm d/2$ above and below that fibre. Two important moments of the stress distribution are the mean stress, $\overline{\sigma}$, and the bending moment, M. They are defined as

$$\overline{\sigma} = \frac{1}{d}\int_{-d/2}^{+d/2} \sigma \, \mathrm{d}z \tag{29}$$

$$M = w\int_{-d/2}^{+d/2} z\sigma\,\mathrm{d}z\,. \tag{30}$$

We are interested in how κ varies at equilibrium when the beam is loaded exclusively by the moment M. As an important boundary condition, there is no axial load. This implies at $\overline{\sigma} = 0$. Solving the stress-strain relation, Eq. (12), for σ, using Eq. (28) for ε and substituting the result for σ in Eq. (29) then yields

$$0 = \frac{1}{d}\int_{-d/2}^{+d/2} Y((z - z_0)\kappa - \eta x)\mathrm{d}z\,. \tag{31}$$

The kernel of the integral contains only constants, except for x and the integration variable z. We can therefore evaluate the integral, obtaining

$$0 = (\eta\bar{x} + \kappa z_0)Y \tag{32}$$

with $\bar{x}$ the mean solute fraction in the beam. Eq. (32) can be solved for the neutral fibre position, which emerges as

$$z_0 = -\frac{\bar{x}\eta}{\kappa}\,. \tag{33}$$

Besides shifting the position of the neutral fiber, changes in the mean solute fraction $\bar{x}$ also entail an expansion or contraction of the beam along its axis.

8.2. Bending-moment curvature relation for linear elasticity

Here we inspect the moment-curvature relation for the "classic" case of linear elasticity and constant composition [59]. With attention to the pure matrix ($x = 0$), we have $\sigma = Y\varepsilon$, $z_0 = 0$, and Eqs. (28) and (30) imply for the moment, M_x, at constant composition the well-known result

$$M_\mathrm{x} = IY\kappa \tag{34}$$

with

$$I = \frac{d^3 w}{12}\,. \tag{35}$$

I is the expression for the area moment of inertia in the present geometry. In the reduced variables of Table 1 (specifically $k = \kappa d$, $y = Y/\theta$), Eq. (34) reads

$$M_\mathrm{x} = \frac{Iy\theta k}{d}\,. \tag{36}$$

Motivated by that expression, a reduced bending moment, $\mathbb{m}$, can be defined as

$$\mathbb{m} = \frac{Md}{I\theta}\,. \tag{37}$$

For the constant-composition case, the moment-curvature relation then takes the simple form

$$\mathbb{m}_\mathrm{x} = yk\,, \tag{38}$$

independent of the beam dimensions.

8.3. Bending at uniform chemical potential

Two variants, illustrated in Fig. 5, of beam bending scenarios at uniform chemical potential are of interest.

- The first is the case of constant and uniform chemical potential, as considered by Larché and Cahn in Ref. [4]. Here, the beam is deformed sufficiently slowly so that the solute can equilibrate with an external reservoir at controlled at constant chemical potential. In other words, solute may be transferred through the external surface of the beam, and the net solute content of the beam may change depending on the curvature.

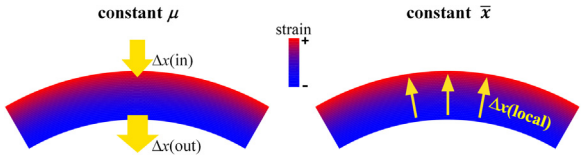

Fig. 5. Schematic representation of solute displacement during beam bending. For constant chemical potential (a), arrows indicate how tensile regions uptake solute from the environment, whereas compressive regions release solute. In general, uptake and release do not cancel and the net composition varies. For constant net composition (b), arrows indicate internal redistribution of solute, here from the compressive towards the tensile fiber. Here, in general, the chemical potential will vary.

- The second variant is the one considered by Gorsky in Ref. [1]. Here, the equilibrium condition is still that of uniform chemical potential throughout the beam. Yet, the net solute content in the beam is considered fixed, in other words, there is no solute transfer through the outer surface of the beam. The chemical potential will then vary as a function of the curvature.

Since the former case has more freedom for redistributing the solute in response to the local loading states, we may expect that case to give the somewhat higher compliance.

8.3.1. Bending at constant chemical potential

We now inspect beam bending for the first of the above two scenarios, namely constant and uniform chemical potential. As the function of the bending curvature, k, we look at the profiles of stress and solute fraction through the beam, and we look at bending moment and mean solute fraction. The underlying numerical procedure is as follows:

- For a given scenario with fixed values of temperature and chemical potential, numerical solutions are successively computed for k starting at 0 and first increasing stepwise to a maximum value, then decreasing stepwise back to 0. The maximum (minimum) solution for x is used in the increasing (decreasing) branch.
- At each k, starting out with an initial guess for the position, ζ_0, of the neutral fibre, the strain at a fixed number (here 200) of sampling points for ζ is computed. This is followed by the determination of x and s at those points, as in Eq. (26). The mean values of x and s are then evaluated as discrete sums approximating the integral in Eq. (29).
- Next, ζ_0 is refined using the result for $\bar{x}$ along with Eq. (33).
- The computation of x and s is then repeated with the updated neutral fibre position.
- This iterative procedure is repeated until the mean stress approximates zero, as decided according to the convergence criterion $|\overline{\sigma}| < 10^{-4}\langle\sigma^2\rangle^{1/2}$. The stress profile then affords computing $\mathbb{m}$ as the discrete sum approximating the integral in Eq. (30).

Fig. 6 exemplifies results of the above procedure. The temperatures, $\tau = 1.1$, 0.9 and 0.7 are selected to probe the three temperature regimes for strain-controlled (as opposed to stress-controlled) deformation, as introduced above. The value of m, namely $+0.01$, positions the stress-free system (at $\tau < 1$) right next to the solvus line of the equilibrium alloy phase diagram, on the side of the concentrated solution.

The following observations are noteworthy:

- At the highest temperature, composition and stress both increase monotonously along the beam thickness (with increasing ζ). Yet, the bending moment for any given curvature is substantially less than at constant composition. Note also that the differential bending stiffness, $\mathrm{d}\mathbb{m}/\mathrm{d}k$, is initially low and then

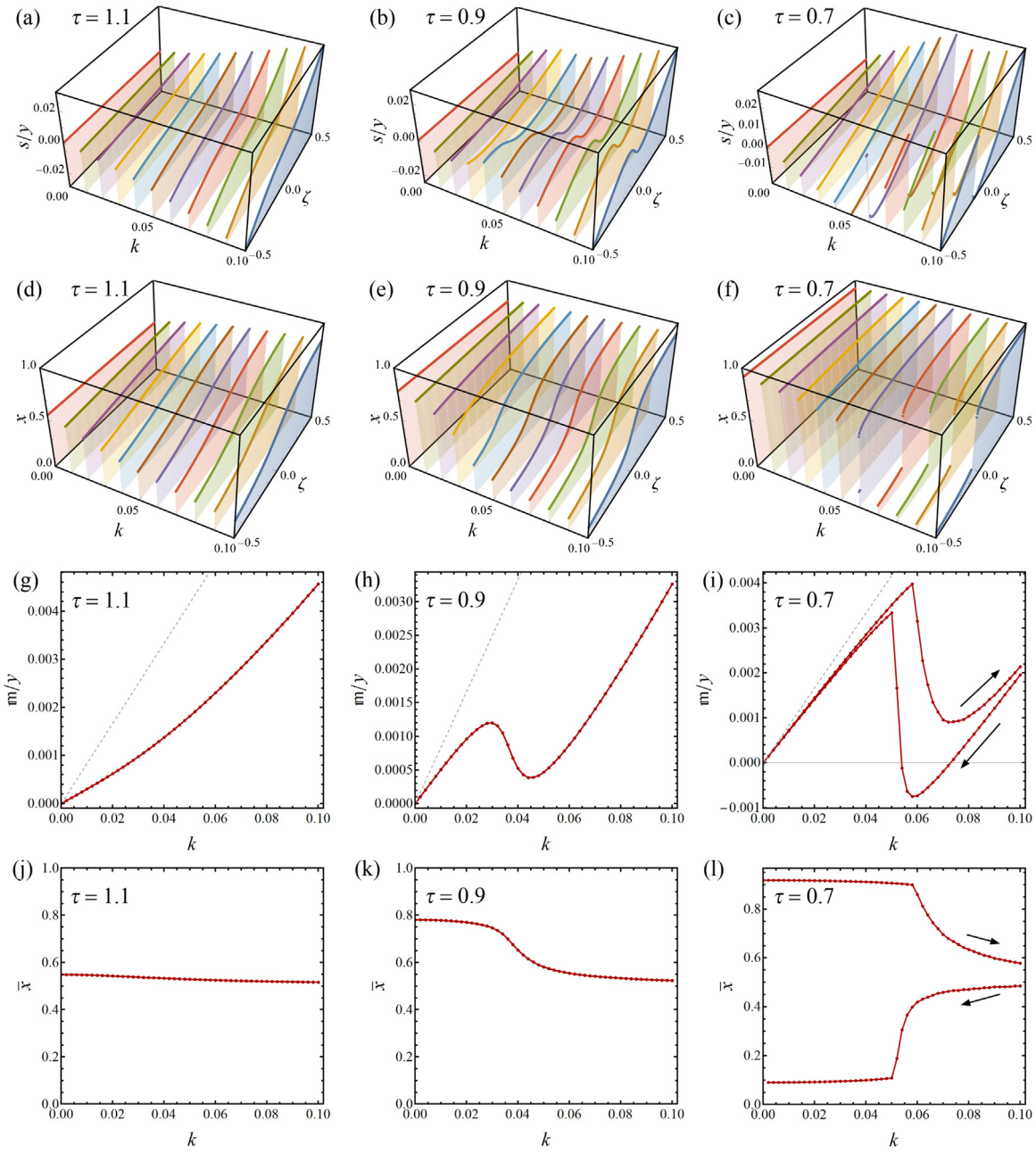

Fig. 6. Variation of stress, bending moment and composition with curvature during beam bending at constant chemical potential (here $m = +0.01$). Reduced temperatures $\tau = 1.1$, 0.9, and 0.7 in left, centre, and right column, respectively and as indicated by labels. (a-c) distribution of stress (normalized to Young's modulus), s/y, over the beam radial coordinate ζ, versus the reduced curvature k. Each line represents the profile at any one of the curvature states investigated. (d–f) distribution of solute fraction, x, in the representation analogous to (a). (g–i) reduced bending moment (normalized to Young's modulus), m/y, versus k. Dashed line: bending at constant composition. (j–l) mean solute fraction versus k. Data in (a–f) refers to sequence of bending starting out with minimum k and (whenever there are two solutions) maximum x, and evolving towards maximum curvature. Data in (g–l) shows also the backwards evolutions, k starting at 0, first increasing and then evolving backwards to 0. Here, where there are two solutions, the one with maximum x is shown in the k-ascending branch and the one with minimum $x$in the k-descending one.

increases as the curvature increases. Furthermore, whereas the strain is by geometry a linear function of the position, the stress variation with ζ is nonlinear.

- At the intermediate temperature, there are points of inflection in the stress-versus-position profile at the higher curvatures. Furthermore, the moment-curvature relation becomes degenerate, with a point of inflection in the graph of moment-versus-curvature. This reflects a similar feature in the graph of $s(\tau, m, \varepsilon)$ for $\tau < 1$, see Fig. 3. The consequence is that the bending scenario with a constant beam curvature along the beam axis will become unstable. Under conditions of prescribed displacement of the end of the beam, the bending could then disproportionate with the beam, along its axis, exhibiting separate regions of low and of high curvature.
- At the lowest temperature, there are jumps in the stress as one moves along ζ. These jumps decorate boundaries between the dilute and concentrated phases. Furthermore, the moment-versus-curvature relation has now developed multiple branches. In Fig. 6(i), this degeneracy includes states with finite bending at zero stress. In other words, there may be states of elastic equilibrium in which the beam remains in a persistent bent configuration even when no moment is applied. Such phenom-

ena would otherwise be considered as reserved for plastic deformation. Yet, all bending is elastic here. Note that the balance of stress that underlies the elastic equilibrium does not automatically imply that the beam is in the lowest energy state. In other words, the state may be metastable but it is not necessarily stable.

Note that the temperature regimes explored in Fig. 6 match those of the alloy phase diagram under conditions of constant stress or constant strain, Fig. 1. In other words, the figure supports the notion that distinct regimes in the alloy phase diagram link to distinctly different elastic behavior of the beam.

8.3.2. Bending at constant mean solute fraction

Here, we inspect beam bending for the second scenario, namely constant mean solute fraction $\bar{x}$ and uniform chemical potential. The neutral fibre position and, thereby, the strain profile are here known a priori (Eq. (33)). However, the value of the chemical potential varies as the function of the curvature. The numerical evaluation is as follows. We assume that the beam has initially been equilibrated at the chemical potential m_0 while the curvature and, consistently, the stress were held at zero. The mean solute fraction, $\bar{x}_0$, is then readily computed by solving Eq. (24) for x at $s = 0$.

- For a given scenario with fixed τ and $\bar{x}_0$, solutions are again successively computed for k starting at 0, with k first increasing stepwise to a maximum value and then decreasing stepwise back to 0. Here again, the maximum (minimum) solution for x is used in the increasing (decreasing) branch.
- Initially, the chemical potential is set to m_0.
- At each k, the composition profile $x(\zeta)$ is computed by solving Eq. (25) for x with the current value of m and at the local value of the strain. The stress profile $s(\zeta)$ is then readily computed based on Eq. (23).
- Next, m is updated by adding $\Delta m = \eta \bar{s}$. This is motivated by the stress-dependence of the chemical potential, Eq. (24), along with the condition that $\bar{s} = 0$ at equilibrium.
- The computation of x and s is then repeated with the new value of m.
- This iterative procedure is repeated until the mean composition agrees with $\bar{x}_0$, as decided according to the convergence criterion that $|\bar{x} - \bar{x}_0|$ be within specified bounds (here: $|\bar{x} - \bar{x}_0| < 0.003\bar{x}_0$).

We found that this procedure provides for efficient convergence, particularly at the higher temperatures.

Fig. 7 exemplifies results for constant $\bar{x}$. The temperatures, $\tau = 1.1$, 0.9 and 0.7 are again selected to probe the 3 temperature regimes for strain-controlled (as opposed to stress-controlled) deformation, as introduced above. Results here show substantially stiffer behavior than for the constant m case.

Two-phase coexistence is here only observed at the lowest temperature, $\tau = 0.7$, at the large-curvature end of the interval under study, and in a very small region of the beam near the most compressed fibre. Its signature on the bending moment m is barely perceptible. It is noteworthy that the signature on the chemical potential m is more pronounced. A closer inspection of that phenomenon has revealed that it reflects the very small sensitivity of the stress to variations in chemical potential of the (prevailing) single-phase states at low temperature. Small variations in m are then compatible with larger variations in m. That same observation also explains the deviation between the m-values of Fig. 7(l) in the two branches representing single-phase states (at low curvature). We have verified that this is numerical error; basing the numerical analysis on the condition of mechanical equilibrium provides more precise solutions for the stress and less precise solutions for the chemical potential.

Fig. 8 explores the composition profiles and the moment-versus curvature relations at different temperature, with a somewhat larger set of τ than above. Part (a) of the figure shows the composition profiles at k =0.10, confirming that the composition profiles are continuous at temperature T_ε ($\tau \approx 0.8$) and above. There is a vertical tangent to $x(\zeta)$ at $T = T_\varepsilon$, and a discontinuity in $x(\zeta)$ – indicating a two-phase state – is only apparent at $T < T_\varepsilon$. The graphs of the bending stiffness in part (b) of the figure shows the softest behavior at $T = T_C$. In fact, vanishing bending stiffness is observed at that temperature and in the limit of small deformation.

8.4. Effective elastic coefficients

We now explore effective elastic coefficients, as they may be obtained by analyzing bending moment-curvature relations such as Fig. 8(b). To this end, $\mathrm{m}(k)$ may be approximated by a Taylor series near $k = 0$. The symmetry of the moment-curvature graph requires that only odd exponents in k contribute. Thus, the expansion takes the form

$$\mathrm{m} = \frac{\mathrm{d}\mathrm{m}}{\mathrm{d}k}\, k + \frac{1}{6}\frac{\mathrm{d}^3\mathrm{m}}{\mathrm{d}k^3}\, k^3 + \mathrm{O}[k^5]\,. \tag{39}$$

In view of Eqs. (34) and (38), the linear coefficient may be identified with an effective (averaged over the beam) Young's modulus. Fig. 9(a) shows that coefficient, as obtained by fitting the data of Fig. 8(b) with Eq. (39), versus the temperature. The comparison, in the figure, with the Larché-Cahn result Eq. (10) shows that the linear coefficients agree closely with the prediction. This is remarkable, since the theory requires constant chemical potential, whereas the numerical data were computed for constant average composition. The agreement suggests that the changes in chemical potential with curvature in that situation do not significantly affect the elastic response in the limit of small curvature.

Specifically, the apparent Young's modulus at the critical temperature is close to zero, as predicted by the theory. At that temperature, the leading behavior in the moment-curvature graph is a third-order polynomial in the curvature.

Fig. 9 (b) displays the third derivatives in Eq. (39) versus the temperature. This data relates to the nonlinearity of the elastic response of the beam, and specifically the third derivatives scale with fourth-order (that is, of the form $\mathrm{d}^4\Psi/\mathrm{d}\varepsilon^4$; for terminology see [60,61]) elastic coefficients, here for the open system. It is seen that the fourth-order coefficient can take either sign, depending on the temperature. Most importantly, the coefficient and, thereby, the nonlinearity of the elastic response of the beam, is largest at the critical temperature.

Larché and Cahn have derived thermodynamic relations for the open system's third-order elastic coefficients [21]. By contrast, theory for the fourth-order coefficients, that could be compared to the data of Fig. 9(b), is not available.

8.5. Spontaneous buckling upon cooling

Mobile solute, such as hydrogen in metals, can encounter barriers for passing the external surface of a sample. The equilibration with an external reservoir of solute may then be slow and equilibria at constant net solute fraction and uniform chemical potential within the solid – as considered in section 8.3.2 above – relevant.

Consider a body that is alloyed at equilibrium in a single-phase region of the alloy phase diagram and that is then cooled into a regime of two-phase coexistence, sufficiently rapid for the net solute fraction to be retained. While the high-temperature state has uniform composition, upon entering the miscibility gap the strife of the chemistry to disproportionate the composition-field into solute-rich and solute-poor regions will compete with the strife of the mechanics to minimize the elastic strain energy with a uniform composition-field. The result can be a spontaneous buckling,

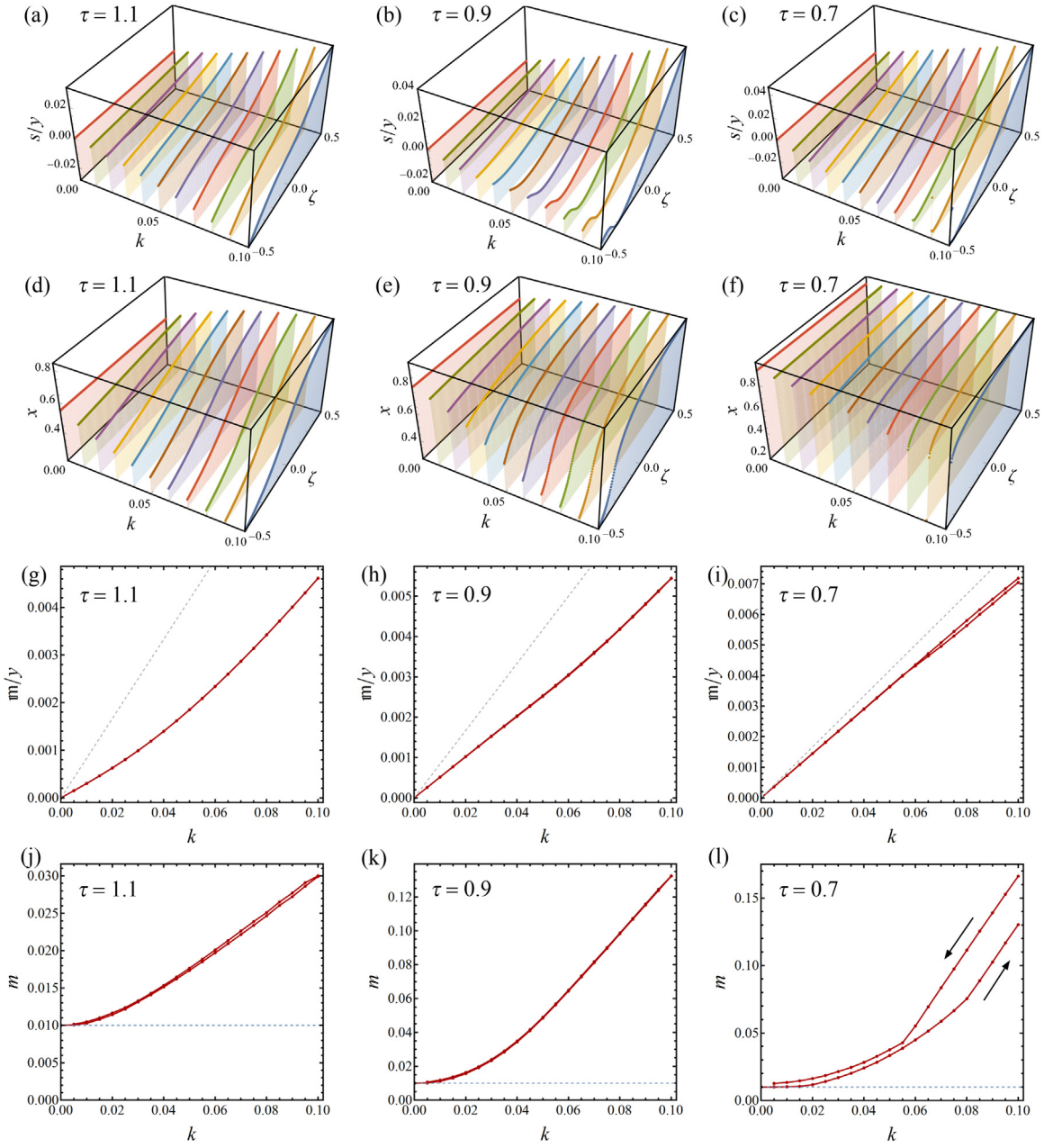

Fig. 7. Variation of stress, composition and chemical potential during beam bending at constant net solute fraction (here for reduced chemical potential m = +0.01 at no stress). Temperatures $\tau = 1.1$, 0.9, and 0.7 in left, centre, and right column, respectively and as indicated by labels. (a–c) distribution of stress (normalized to Young's modulus), s/y, over the beam radial coordinate ζ, versus the reduced curvature k. Each line represents the profile at any one of the curvature states investigated. (d–f) distribution of solute fraction, x, in the representation analogous to (a). (g–i) reduced bending moment (normalized to Young's modulus), $\mathfrak{m}/y$, versus k. Dashed line: bending at constant composition. (j–l) mean solute fraction versus k. Data in (a–f) refers to sequence of bending starting out with minimum k and (whenever there are two solutions) maximum x, and evolving towards maximum curvature. Data in (g–l) shows also the backwards evolutions, k starting at 0, first increasing and then evolving backwards to 0. Here, where there are two solutions, the one with maximum x is shown in the k-ascending branch and the one with minimum $x$in the k-descending one.

with a strain field that will generally depend on the geometry of the body.

Fig. 10 exemplifies the above scenario for a beam that is equilibrated, at $\tau > 1$, with a reservoir at $m = 0$, so that $x = 1/2$. The beam is then cooled into the miscibility gap at $\tau < 1$, in the absence of an applied bending moment and keeping the net solute fraction constant. Next, the beam is bent at uniform m and the moment recorded. In part (a) of the figure, it is seen that the moment-curvature relations at $\tau < 1$ have segments in the unstable regions of the diagram. Here, the zero crossings at $k \neq 0$ correspond to stable states of finite curvature at no external load. In other words, the beam will spontaneously buckle upon cooling. Fig. 10(b) exemplifies associated composition profiles.

9. Relation between global uniaxial deformation of networks and local bending of struts

Several studies have reported an enhanced elastic compliance of bulk metal hydrides when alloyed with hydrogen [62–66], and observations of the elastic aftereffect in cantilevers or foils have been discussed as the consequence of hydrogen relocation in stress gradients [2,15,67]. Yet, the only quantitative verification of

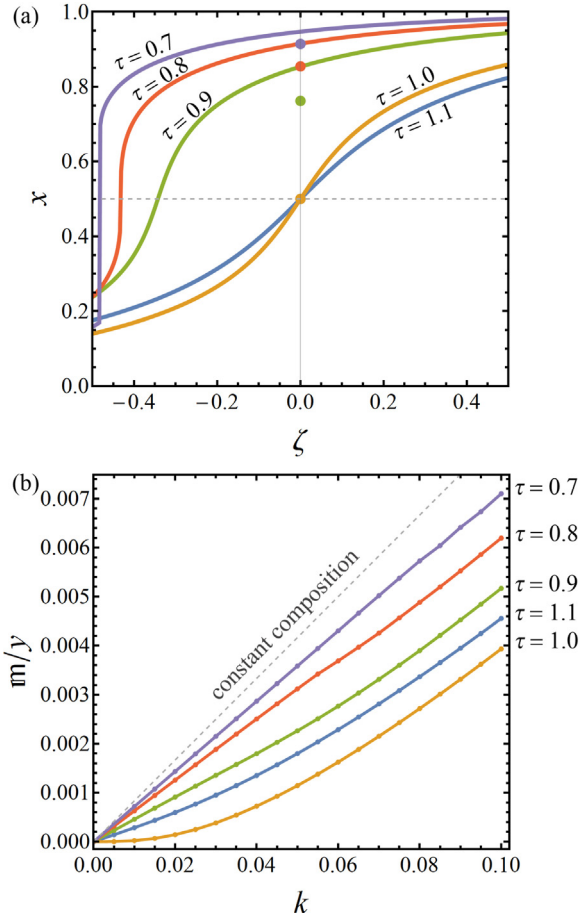

Fig. 8. Variation of moment and composition during beam bending at constant net solute fraction (here in each case for reduced chemical potential $m = 0$ at no stress), for various temperatures. (a) solute fraction versus position at reduced curvature $k = 0.10$. (b) moment versus curvature. Full circles in (a): net solute fraction (blue hidden underneath yellow). Color code: reduced temperature $\tau = 1.1$ - blue; 1.0 - yellow; 0.9 - green; 0.8 - red; 0.7 - violet. Note softest behaviour at critical temperature, $\tau = 1.0$. Dashed line in (b): bending at constant composition. (For interpretation of the references to color in this figure legend, the reader is referred to the web version of this article.)

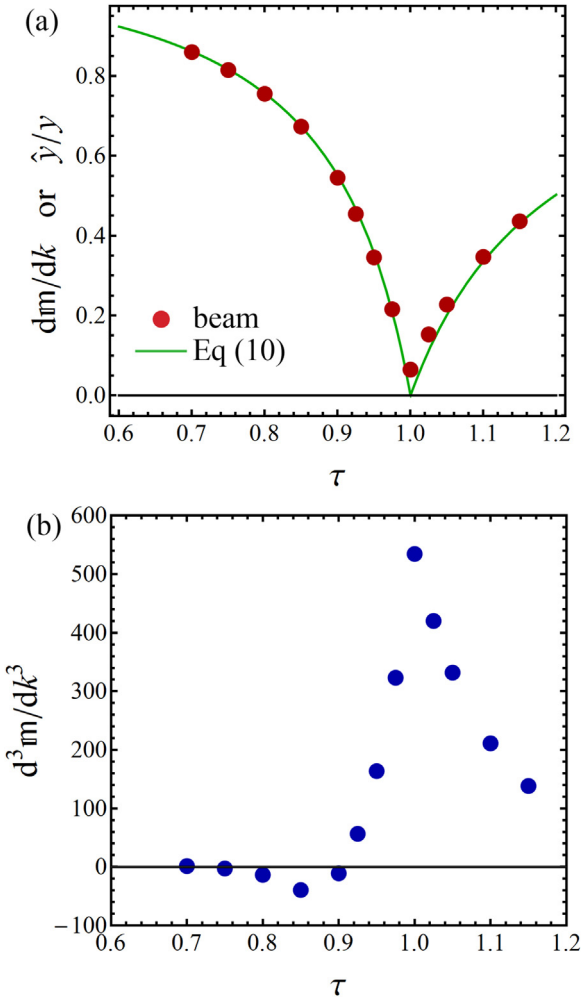

Fig. 9. Series expansion coefficients (see Eq. (39)) versus reduced temperature τ for the bending moment–curvature relations of Fig. 8. (a), linear coefficient, $\mathrm{d}\mathfrak{m}/\mathrm{d}k$, (symbols) and the prediction by Larché and Cahn for the reduced open-system Young's modulus (normalized to the closed system one), $\hat{y}/y$. Note the excellent agreement. (b), third-order coefficient, $\mathrm{d}^3\mathfrak{m}/\mathrm{d}k^3$.

the Larché-Cahn theory of open system elasticity has been based on experiments with nanoporous metal made by dealloying [14]. That study also advertised the opportunities of using hydrogen in nanoporous metals for generating materials with switchable effective elasticity, including states with near zero Young's modulus.

In this Section, we explore the question: how do the considerations on the bending of individual beams relate to experiments–such as Ref [14]–on dealloyed nanoporous metal? Specifically, for any given value of the macroscopic uniaxial deformation of a nanoporous metal sample, how much bending magnitude should we expect locally, in the struts that form the nanoporous metal?

Dealloyed nanoporous metals may be considered as networks of struts [18]. At sufficiently low solid fraction, the macroscopic effective elastic response to uniaxial load is carried, locally, by bending of the network struts [17]. We derive a relation between the macroscopic strain, ϵ, and a mean magnitude of the local curvature by analysis of the strain energy density. We shall restrict the analysis to the limit of small strain and, hence, linear elasticity. In other words, we shall ignore higher order elastic coefficients. The local elastic response is then governed by the value of Young's modulus. That quantity may represent the closed or the open system, without consequences for the analysis here.

In terms of the effective macroscopic Young's modulus, Y^{eff}, the macroscopic strain energy density, per volume of the solid phase in the porous solid, is

$$\Psi^{\mathrm{macro}} = \frac{1}{2\varphi} Y^{\mathrm{eff}} \epsilon^2 \,, \tag{40}$$

with φ the solid volume fraction of the porous material. For dealloyed nanoporous metal with $\varphi < 0.5$, the modulus Y^{eff} can be approximated as (Shi et al. [20], Soyarslan et al. [68])

$$Y^{\mathrm{eff}} = 2Y \left(\frac{\varphi - \varphi_{\mathrm{perc}}}{1 - \varphi_{\mathrm{perc}}} \right)^{5/2} \,, \tag{41}$$

with φ_{perc} the solid fraction at the percolation limit, here 0.159 [68]. Locally, in the curved beams, the strain energy density (energy per volume of the beam, averaged over the cross-section) is

$$\Psi^{\mathrm{bending}} = \frac{1}{wd} \int_{-d/2}^{+d/2} \frac{1}{2} Y \kappa^2 z^2 w \mathrm{d}z = \frac{1}{24} d^2 \kappa^2 Y. \tag{42}$$

Since both deformations are elastic and, hence, conservative and reversible, the strain energy densities must (on average) be equal. This suggests equating Ψ^{macro} (Eq. (40)) and the mean of Ψ^{bending} (Eq. (42)) and solving for the curvature. In this way, and

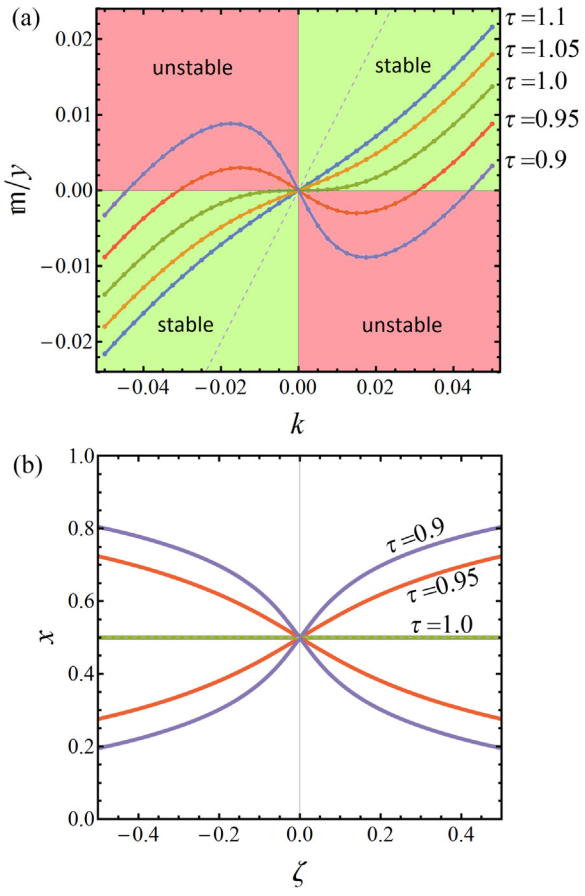

Fig. 10. Spontaneous buckling of a beam upon cooling into a two-phase regime of the phase diagram. Graphs consider a beam that was alloyed to equilibrium at reduced chemical potential $m = 0$ and reduced temperature $\tau > 1$, that is to net solute fraction $x = 1/2$. The beam was then cooled at constant overall solute fraction. (a), reduced moment (normalized to Young's modulus) $\mathfrak{m}/y$ versus reduced curvature k at various temperatures. Note that graphs for $\tau < 1$ have segments in the upper left and lower right quadrants, which correspond to unstable states. For $\tau < 1$, the zero crossings at $\mathfrak{m} \neq 0$ here correspond to stable states of nonzero curvature at no applied load, in other words to spontaneous buckling. Dashed: linear stress-strain relation at constant composition. (b) composition profiles for the stable states.

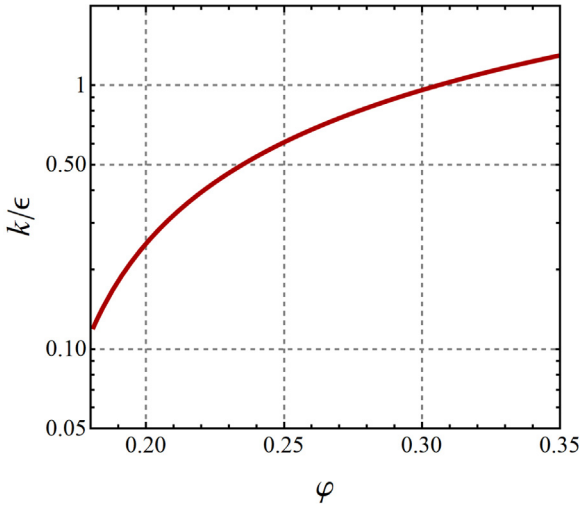

Fig. 11. Ratio, k/ϵ, between the root-mean-square of the reduced curvature, $k = \kappa d$, and the macroscopic strain, ϵ, of a porous solid, plotted versus the solid fraction, φ.

accounting for $k = \kappa d$, one readily finds that

$$\frac{\sqrt{\langle k^2 \rangle}}{\epsilon} = 2\sqrt{\frac{6}{\varphi}}\left(\frac{\varphi - \varphi_{\text{perc}}}{1 - \varphi_{\text{perc}}}\right)^{5/4}, \tag{43}$$

where $\langle\rangle$ denotes an average over all struts.

Fig. 11 shows the prediction of Eq. (43) for how the ratio (left-hand side of the equation) between the root-mean-square (RMS) of the local reduced curvatures k of the struts and the macroscopic strain, ϵ of a porous solid, varies with the solid fraction, φ. Dealloyed nanoporous metals typically have $\varphi = 0.2$–0.3. The ratio is then $k/\varepsilon \sim 0.25$–1. In other words, the macroscopic strain ϵ and the RMS reduced curvature k are of comparable magnitude. In that sense, the results of our analysis of the bending of isolated beams may be transferred to the macroscopic deformation behavior of nanoporous metal.

10. Discussion and summary

We have analyzed the elastic response of bars of a solid solution under axial loading and in bending. The composition was allowed to change so as to keep the chemical potential, μ, constant and/or uniform at equilibrium. As compared to linear elastic beams at constant composition, the elastic response at uniform μ exhibits a surprisingly rich phenomenology.

Beams at axial load have a monotonously increasing but nonlinear stress-strain graph at high temperature. At the critical temperature, the stress-strain graph develops a horizontal tangent that corresponds to a state of vanishing rigidity. This state can be encountered even when the value of μ differs from that of the critical point. At even lower temperature, the deformation may trigger a phase transformation. There is then an extended region in the stress-strain domain where the solid solution is in a two-phase state. The material can here go through extended intervals of strain while the stress remains constant.

Finite intervals of strain at constant stress are also encountered in "superelastic" materials including shape memory alloys and gum metal, where the stress triggers a martensitic and diffusionless phase transformation while the composition remains constant [69–71]. The present phenomenology is similar, yet the phase transformation is here not martensitic. Instead, it is accompanied by a finite change in composition that requires diffusion.

Whereas axial loading is characterized by uniform stress along the beam, bending at prescribed curvature implies prescribed values of the strain (gradient) in the cross-section of the beam. The different mechanical boundary conditions, prescribed stress versus prescribed strain, have ramifications for the chemistry, and specifically they are reflected in the alloy phase diagram. Depending on the control variable, stress or strain, one encounters two separate – and in each case well-defined and predictable – upper convolute temperatures of the miscibility gap. That distinction is reflected in the elastic response of the open system.

We have considered two variants of the bending of beams under conditions of uniform chemical potential: the first condition holds the chemical potential constant, irrespective of the bending curvature. Bending will then be accompanied by a change in the net solute content of the beam, in other words, exchange of solute with an external reservoir through the surface of the beam. The second condition holds the net solute content constant (no exchange through the surface), but allows for solute relocation between the tensile and compressive fiber of the beam. Here, the chemical potential varies along with the bending radius.

When bent at constant μ and intermediate temperature, the beam can experience regimes of the curvature were the bending-moment curvature relation has an instability. Deformation with, for instance, the displacement of the free end of a cantilever prescribed will then lead to states in which the curvature is not a

constant along the beam axis. At low temperature, there can be two-phase states, including the possibility that the beam remains locked-in to a state of finite curvature even when the acting bending moment is entirely removed. Furthermore, alloy beams at constant net solute fraction and no load may spontaneously buckle when quenched into the two-phase regime of the alloy phase diagram. The buckling reflects regions of elastic instability in parameter space, where $\hat{Y} < 0$.

Bending at constant overall solute content provides for a stiffer moment-curvature relation than at constant μ. Yet, in each case the bending stiffness will still approximate zero at the critical temperature. At that temperature, the nonlinearity of the elastic response (which is governed by a fourth order, open-system elastic coefficient) is at maximum, and the bending moment depends on the curvature to third order as the leading term. There is then a finite interval in curvature with extremely small bending stiffness or, in other words, giant bending compliance. The stiffness will then rapidly increase at higher curvatures.

With an eye on experiments using dealloyed nanoporous or network materials for probing the open-system elastic response, we have investigated in how far the mean local bending of the struts in the network reflects the macroscopic axial elastic deformation. The two measures for the deformation are found of comparable magnitude. This suggests that the observations of the present work can be reflected in the macroscopic elastic response of a network material and under experimental conditions that can be realized by proper choice of chemical potential, temperature, and load. That finding is significant, as the open-system elastic response has been poorly explored in experiment so far, and as its phenomenology includes such potentially interesting properties as an elastic response that can be switched under control of the chemical potential, specifically in such a way that states of extremely low rigidity or bistable elastic behavior can be selected on demand by the experimentalist.

Declaration of Competing Interest

None.

Acknowledgement

This work was supported by the German Research Foundation (DFG) through grant WE1424/18-1.

References

[1] W. Gorsky, Theorie der Elastischen Nachwirkung in ungeordneten Mischkristallen (elastische Nachwirkung zweiter Art), Phys. Z. Sowjetunion 8 (1935) 457–471.
[2] J. Völkl, The Gorsky effect, Ber. Bunsenges. Phys.Chem. 76 (8) (1972) 797–805.
[3] H. Wipf, Diffusion of hydrogen in metals, in: H. Wipf (Ed.), Hydrogen in Metals III: Properties and Applications, Topics in Applied Physics, vol. 73, 1997, pp. 51–91.
[4] F. Larché, J.W. Cahn, A linear theory of thermochemical equilibrium of solids under stress, Acta Metall. 21 (8) (1973) 1051–1063.
[5] H. Callen, Thermodynamics and an Introduction to Thermostatistics, Wiley, New York, 1985.
[6] P.H. Leo, R.F. Sekerka, The effect of elastic fields on the morphological stability of a precipitate grown from solid-solution, Acta Metall. 37 (12) (1989) 3139–3149.
[7] M.E. Thompson, C.S. Su, P.W. Voorhees, The equilibrium shape of a misfitting precipitate, Acta Metall. Mater. 42 (6) (1994) 2107–2122.
[8] P. Fratzl, O. Penrose, J.L. Lebowitz, Modeling of phase separation in alloys with coherent elastic misfit, J. Stat. Phys. 95 (5–6) (1999) 1429–1503.
[9] R. Mukherjee, T.A. Abinandanan, M.P. Gururajan, Phase field study of precipitate growth: effect of misfit strain and interface curvature, Acta Mater. 57 (13) (2009) 3947–3954.
[10] M. McDowell, S. Lee, W. Nix, Y. Cui, 25th anniversary article: understanding the lithiation of silicon and other alloying anodes for lithium-ion batteries, Adv. Mater. 25 (36) (2013) 4966–4984.
[11] L. Chen, F. Fan, L. Hong, J. Chen, Y.Z. Ji, S.L. Zhang, T. Zhu, L.Q. Chen, A phase–field model coupled with large elasto-plastic deformation: application to lithiated silicon electrodes, J. Electrochem. Soc. 161 (11) (2014) F3164–F3172.
[12] Y. Mishin, Calculation of open and closed system elastic coefficients for multicomponent solids, Phys. Rev. B 91 (22) (2015) 224107.
[13] J. Park, R.D. Kamachali, S.-D. Kim, S.-H. Kim, C.-S. Oh, C. Schwarze, I. Steinbach, First evidence for mechanism of inverse ripening from in-situ TEM and phase–field study of δ' precipitation in an Al-Li alloy, Sci. Rep. 9 (1) (2019) 3981.
[14] S. Shi, J. Markmann, J. Weissmüller, Verifying Larché–Cahn elasticity, a milestone of 20th-century thermodynamics, Proc. Natl. Acad. Sci. 115 (43) (2018) 10914–10919.
[15] G. Alefeld, G. Schaumann, J. Tretkowski, J. Völkl, Ferroelasticity of niobium due to hydrogen as a lattice gas, Phys. Rev. Lett. 22 (14) (1969) 697.
[16] J. Völkl, G. Alefeld, The gorsky effect: recent results, Il Nuovo Cimento B (1971–1996) 33 (1) (1976) 190–204.
[17] N. Huber, R.N. Viswanath, N. Mameka, J. Markmann, J. Weißmüller, Scaling laws of nanoporous metals under uniaxial compression, Acta Mater. 67 (0) (2014) 252–265.
[18] H.-J. Jin, J. Weissmüller, D. Farkas, Mechanical response of nanoporous metals: a story of size, surface stress, and severed struts, MRS Bull. 43 (1) (2018) 35–42.
[19] L.-Z. Liu, Y.-Y. Zhang, H. Xie, H.-J. Jin, Transition from homogeneous to localized deformation in nanoporous gold, Phys. Rev. Lett. 127 (9) (2021) 095501.
[20] S. Shi, Y. Li, B.-N. Ngo-Dinh, J. Markmann, J. Weissmüller, Scaling behavior of stiffness and strength of hierarchical network nanomaterials, Science 371 (6533) (2021) 1026.
[21] F. Larche, J.W. Cahn, Non-linear theory of thermochemical equilibrium of solids under stress, Acta Metall. 26 (1) (1978) 53–60.
[22] W.-L. Chen, K.R. Shull, T. Papatheodorou, D.A. Styrkas, J.L. Keddie, Equilibrium swelling of hydrophilic polyacrylates in humid environments, Macromolecules 32 (1) (1999) 136–144.
[23] M.S. Dimitriyev, Y.-W. Chang, P.M. Goldbart, A. Fernández-Nieves, Swelling thermodynamics and phase transitions of polymer gels, Nano Futures 3 (4) (2019) 042001.
[24] P. Fratzl, F.G. Barth, Biomaterial systems for mechanosensing and actuation, Nature 462 (7272) (2009) 442–448.
[25] A. Mukhopadhyay, B.W. Sheldon, Deformation and stress in electrode materials for li-ion batteries, Prog. Mater. Sci. 63 (2014) 58–116.
[26] G. Alefeld, Hydrogen in Metals I - Basic Properties, Topics in Applied Physics,, vol. 28, Springer, Berlin, 1978..
[27] J.V. G. Alefeld, Hydrogen in Metals II - Application Oriented Properties, Topics in Applied Physics,, vol. 29, Springer, Berlin, 1978..
[28] B. Baranowski, S. Majchrzak, T. Flanagan, The volume increase of fcc metals and alloys due to interstitial hydrogen over a wide range of hydrogen contents, J. Phys. F 1 (3) (1971) 258.
[29] E. Wicke, H. Brodowsky, H. Züchner, Hydrogen in palladium and palladium alloys, in: J. Alefeld, G. Völkl (Eds.), Hydrogen in Metals II, vol. 29, Springer Berlin Heidelberg, Berlin, Heidelberg, 1978, pp. 73–155.
[30] H. Peisl, Lattice strains due to hydrogen in metals, in: G. Alefeld, J. Völkl (Eds.), Hydrogen in Metals I, vol. 28, Springer, Berlin, Heidelberg, 1978, pp. 69–70.
[31] T. Kuji, W. Oates, Thermodynamic properties of Nb-H alloys III: calculation of part of the phase diagram, J. Less Common. Metals 102 (2) (1984) 273–279.
[32] H. Brodowski, Das System Palladium/Wasserstoff, Z. Phys. Chem. Neue Folge 44 (1965) 129–142.
[33] J. Bonet, R.D. Wood, Nonlinear Continuum Mechanics for Finite Element Analysis, Cambridge University Press, Cambridge; New York, NY, 2008.
[34] F.C. Larche, J.W. Cahn, Thermochemical equilibrium of multiphase solids under stress, Acta Metall. 26 (10) (1978) 1579–1589.
[35] N.F. Mott, F.R.N. Nabarro, An attempt to estimate the degree of precipitation hardening, with a simple model, Proc. Phys. Soc. 52 (1) (1940) 86.
[36] J.D. Eshelby, The Continuum Theory of Lattice Defects, vol. 3, Academic Press, 1956, pp. 79–144.
[37] J.M. López, J.A. Alonso, The atomic size-mismatch contribution to the enthalpy of formation of concentrated substitutional metallic solid solutions, Phys. Status Solidi (a) 85 (2) (1984) 423–428.
[38] F.R.d. Boer, W.C.M. Mattens, R. Boom, A.R. Miedema, A.K. Niessen, Cohesion in Metals, North-Holland, Netherlands, 1988.
[39] R. Darvishi Kamachali, L. Wang, Elastic energy of multi-component solid solutions and strain origins of phase stability in high-entropy alloys, Scr. Mater. 206 (2022) 114226.
[40] D.A. Porter, K.E. Easterling, M. Sherif, Phase Transformations in Metals and Alloys, third ed., CRC Press, Boca Raton FL, 2009.
[41] C. Wagner, Contribution to the thermodynamics of interstitial solid solutions, Acta Metall. 19 (8) (1971) 843–849.
[42] T.B. Flanagan, W. Oates, The palladium-hydrogen system, Annu. Rev. Mater. Sci. 21 (1) (1991) 269–304.
[43] E. Brandes, G. Brook, Smithells Metals Reference Book, Elsevier, Butterworth-Heinemann, Oxford, 2013.
[44] H. Frieske, E. Wicke, Magnetic susceptibility and equilibrium diagram of PdH_n, Ber. Bunsenges. Phys.Chem. 77 (1) (1973) 48–52.
[45] J.W. Arblaster, Crystallographic properties of palladium, Platin. Met. Rev. 56 (3) (2012) 181–189.
[46] T.B. Massalski, H. Okamoto, P.R. Subramanian, L. Kacprzak, Binary Alloy Phase Diagrams, ASM International, Materials Park, OH, 1990.
[47] S. Shi, J. Markmann, J. Weissmüller, Actuation by hydrogen electrosorption in hierarchical nanoporous palladium, Philos. Mag. 97 (2017) 1571–1587.
[48] J.W. Cahn, On spinodal decomposition, Acta Metall. 9 (9) (1961) 795–801.
[49] W.C. Johnson, P.W. Voorhees, Phase equilibrium in two-phase coherent solids, Metall. Trans. A 18 (7) (1987) 1213–1228.

[50] Z.-K. Liu, J. Ågren, On two-phase coherent equilibrium in binary alloys, Acta Metall. Mater. 38 (4) (1990) 561–572.
[51] R.B. Schwarz, A.G. Khachaturyan, Thermodynamics of open two-phase systems with coherent interfaces: application to metal-hydrogen systems, Acta Mater. 54 (2) (2006) 313–323.
[52] A. Weidinger, D. Nagengast, C. Rehm, F. Klose, B. Pietzak, Metallic multilayers and hydrogen, Thin Solid Films 275 (1–2) (1996) 48–53.
[53] S. Wagner, A. Pundt, Quasi-thermodynamic model on hydride formation in palladium-hydrogen thin films: impact of elastic and microstructural constraints, Int. J. Hydrog. Energy 41 (4) (2016) 2727–2738.
[54] S. Wagner, P. Klose, V. Burlaka, K. Nörthemann, M. Hamm, A. Pundt, Structural phase transitions in niobium hydrogen thin films: mechanical stress, phase equilibria and critical temperatures, Chemphyschem 20 (14) (2019) 1890–1904.
[55] J. Weissmüller, C. Lemier, On the size dependence of the critical point of nanoscale interstitial solid solutions, Philos. Mag. Lett. 80 (6) (2000) 411–418.
[56] A. Baldi, T.C. Narayan, A.L. Koh, J.A. Dionne, In situ detection of hydrogen-induced phase transitions in individual palladium nanocrystals, Nat. Mater. 13 (12) (2014) 1143–1148.
[57] M. Doi, Elasticity effects on the microstructure of alloys containing coherent precipitates, Prog. Mater. Sci. 40 (2) (1996) 79–180.
[58] S. Wagner, H. Uchida, V. Burlaka, M. Vlach, M. Vlcek, F. Lukac, J. Cizek, C. Baehtz, A. Bell, A. Pundt, Achieving coherent phase transition in palladium-hydrogen thin films, Scr. Mater. 64 (10) (2011) 978–981.
[59] W.C. Young, R.G. Budynas, A.M. Sadegh, Roark's Formulas for Stress and Strain, McGraw-Hill Education, 2012.
[60] F. Birch, Finite elastic strain of cubic crystals, Phys. Rev. 71 (11) (1947) 809–824.
[61] H. Wang, M. Li, Ab initio calculations of second-, third-, and fourth-order elastic constants for single crystals, Phys. Rev. B 79 (22) (2009) 224102.
[62] D.K. Hsu, R.G. Leisure, Elastic constants of palladium and β-phase palladium hydride between 4 and 300 K, Phys. Rev. B 20 (1979) 1339–1344.
[63] K. Salama, C.R. Ko, Effect of hydrogen on the temperature dependence of the elastic constants of palladium single crystals, J. Appl. Phys. 51 (1980) 6202–6209.
[64] M. Sandys-Wunsch, F.D. Manchester, Spinodal temperatures for macroscopic density fluctuations in Pd–H. II. Elastic constants above the critical point, J. Phys. 4 (1992) 2149.
[65] R. Schwarz, H. Bach, U. Harms, D. Tuggle, Elastic properties of Pd–hydrogen, Pd–deuterium, and Pd–tritium single crystals, Acta Mater. 53 (3) (2005) 569–580.
[66] D. Safarik, R. Schwarz, S. Paglieri, R. Quintana, D. Tuggle, D. Byler, Composition dependence of the elastic constants of β-phase and $(\alpha+\beta)$-phase PdH_x, Ultrasonics 50 (2010) 155–160.
[67] K. Kandasamy, F.A. Lewis, Important Gorsky effect influences on diffusion coefficients in metal-hydrogen systems, Int. J. Hydrog. Energy 24 (8) (1999) 763–769.
[68] C. Soyarslan, S. Bargmann, M. Pradas, J. Weissmüller, 3D stochastic bicontinuous microstructures: generation, topology and elasticity, Acta Mater. 149 (5) (2018) 326–340.
[69] T.W. Duerig, The use of superelasticity in modern medicine, MRS Bull. 27 (2) (2002) 101–104.
[70] R.J. Talling, R.J. Dashwood, M. Jackson, D. Dye, On the mechanism of superelasticity in gum metal, Acta Mater. 57 (4) (2009) 1188–1198.
[71] J. Mohd Jani, M. Leary, A. Subic, M.A. Gibson, A review of shape memory alloy research, applications and opportunities, Mater. Des. (1980–2015) 56 (2014) 1078–1113.